**Weierstraß-Institut**
**für Angewandte Analysis und Stochastik**

**Leibniz-Institut im Forschungsverbund Berlin e. V.**

Preprint ISSN 2198-5855

# Impact of viscosity modeling on the simulation of aortic blood flow

Sarah Katz[1], Alfonso Caiazzo[1], Volker John[1,2]

submitted: 24th October 2022

[1] Weierstraß-Institut
Mohrenstr. 39
10117 Berlin
E-Mail: sarah.katz@wias-berlin.de
alfonso.caiazzzo@wias-berlin.de
volker.john@wias-berlin.de

[2] Freie Universität Berlin
Arnimallee 6
14195 Berlin

No. 2963
Berlin 2022

2020 *Mathematics Subject Classification.* 76A05, 76-10, 76M10.

*Key words and phrases.* Computational hemodynamics, finite element method, viscosity modeling, non-Newtonian fluids, turbulence modeling.

The work of S. Katz has been supported by the Deutsche Forschungsgemeinschaft (DFG) within the RTG 2433 *Differential Equation- and Data-driven Models in Life Sciences and Fluid Dynamics (DAEDALUS)*. The geometry and the time-averaged flow data were provided by Prof. Dr. L. Goubergrits & J. Brüning, Institute of Computer-assisted Cardiovascular Medicine, Charité – Universitätsmedizin Berlin.

Edited by
Weierstraß-Institut für Angewandte Analysis und Stochastik (WIAS)
Leibniz-Institut im Forschungsverbund Berlin e. V.
Mohrenstraße 39
10117 Berlin
Germany

Fax: +49 30 20372-303
E-Mail: preprint@wias-berlin.de
World Wide Web: http://www.wias-berlin.de/

# Impact of viscosity modeling on the simulation of aortic blood flow

Sarah Katz, Alfonso Caiazzo, Volker John

**Abstract**

Modeling issues for the simulation of blood flow in an aortic coarctation are studied in this paper. From the physical point of view, several viscosity models for non-Newtonian fluids as well as a Newtonian fluid model will be considered. From the numerical point of view, two different turbulence models are utilized in the simulations. The impact of both, the physical and the numerical modeling, on clinically relevant biomarkers is investigated and compared.

## 1 Introduction

The severity of heart diseases can be assessed by several biomarkers. For instance, the most relevant clinical parameter for coarctation of the aorta is the trans-stenotic pressure difference. However, this quantity can be measured directly only by an invasive catheterization. Medical imaging, e.g., cardiac MRI, is a pillar of clinical diagnostic techniques and can give valuable information [1]. Nevertheless the resolution of the images is not always sufficient to determine all desired biomarkers with the required accuracy. To this end, numerical simulations are an indispensable tool for supporting available data with predictions for clinically relevant quantities of interest, e.g., see [2, 3].

This paper will continue the study of turbulent blood flow simulations through a stenotic aorta begun in [4]. For simulating a complex process, several decisions on the physical and numerical modeling have to be made. Two aspects to be taken into account for blood flow simulations are as follows. First, blood is certainly a non-Newtonian fluid, such that using a Newtonian model, as in [4], is only an approximation. Second, the aorta is certainly not a rigid body, such that neglecting the fluid-structure interactions of the flow and the wall of the aorta, as in [4], is a simplifying modeling approach. The impact of such simplifications on the quantities of interest is a question of central concern. This question will be studied in the present paper for the first aspect. To this end, several viscosity models leading to non-Newtonian fluids, as previously applied to blood flow simulations in [5, 6, 7, 8, 9], will be studied for the flow in an aortic coarctation.

Having fixed the model for the physical process, a numerical model has to be applied for the simulation. In the simplest case, a standard discretization, e.g., a Galerkin finite element method in space, is sufficient. However, the flow in larger blood vessels such as the aorta is turbulent. Most of the small flow scales cannot be represented on affordable grids and their impact on the resolved scales has to be modeled via a turbulence model. The impact of different turbulence models on clinically relevant biomarkers, in the context of a Newtonian fluid model, is investigated in [4]. As shown in this paper, the turbulence models can be classified in two main groups, depending on the amount of numerical viscosity introduced by the model. In the present paper, one model from each group is considered. With this setup, it will be studied whether the viscosity modeling or the turbulence modeling possess a larger impact on the prediction of the biomarkers.

DOI 10.20347/WIAS.PREPRINT.2963 Berlin 2022

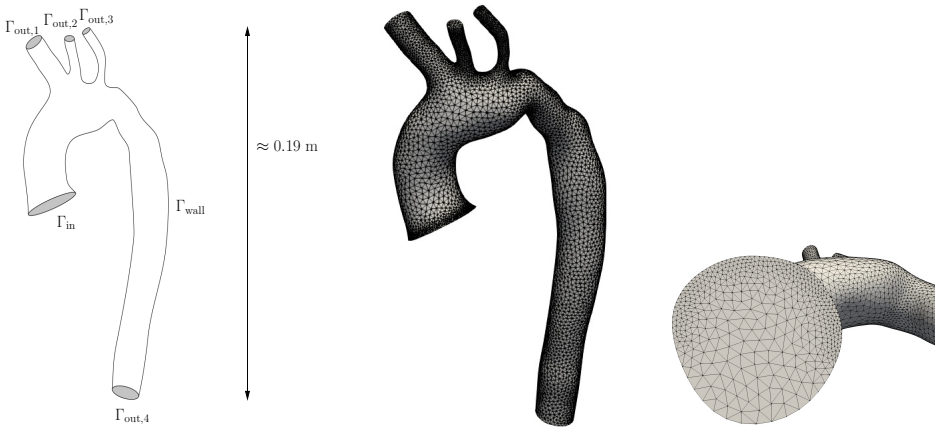


Figure 1: Left: Sketch of the computational domain, representing a segment of the aorta, and the corresponding decomposition of the boundary. Center and right: Surface mesh $\mathcal{T}$, and zoom on the inlet boundary $\Gamma_{\text{in}}$.

The paper is organized as follows. Section 2 describes the physical and numerical modeling, providing in particular details to the used viscosity models and turbulence models. The clinically relevant quantities of interest, which are monitored in the simulations, are explained in Section 3. Section 4 presents the results of our numerical simulations, which are summarized in Section 5.

# 2 Modeling

This section introduces the governing continuous and discrete equations considered for the aortic blood flow, in particular focusing on the different models for the viscosity, the applied discretizations in time and space as well as the considered turbulence models.

## 2.1 Blood Flow Modeling

Figure 1 (left) depicts the computational domain $\Omega \subset \mathbb{R}^3$, representing a piece of a patient's aorta segmented from medical imaging. See [4] for more details on the acquisition of the data. The inlet $\Gamma_{\text{in}}$ was chosen immediately above the sinotubular junction; the positions of the outlets are, in order:

$\Gamma_{\text{out},1}$: about $25\,\text{mm}$ along the brachiocephalic artery, prior to its division into the right subclavian and right common carotid arteries,

$\Gamma_{\text{out},2}$: about $25\,\text{mm}$ along the left common carotid artery,

$\Gamma_{\text{out},3}$: about $30\,\text{mm}$ along the left subclavian artery, and

$\Gamma_{\text{out},4}$: the descending aorta at the level of the left ventricular apex.

The total length of the considered aorta segment is roughly $25\,\text{cm}$.

We model the blood flow in $\Omega$ as an incompressible, generalized Newtonian fluid, whose dynamics is described by the incompressible Navier–Stokes equations in terms of a velocity field $\boldsymbol{u}\,[\text{m}/\text{s}] : \Omega \to \mathbb{R}^3$

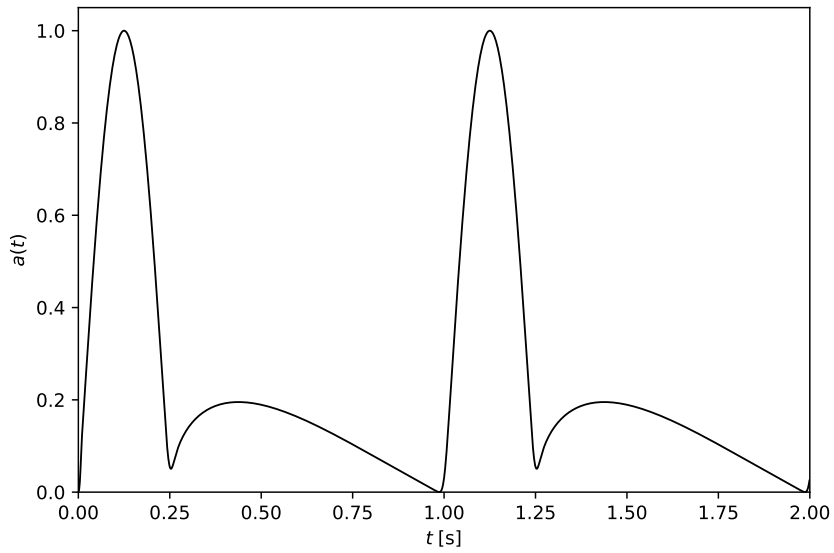


Figure 2: Relative inflow amplitude over time, first two periods.

and a pressure field $p\ [\mathrm{Pa}] : \Omega \to \mathbb{R}$ satisfying the system of equations

$$\begin{aligned} \rho\partial_t \boldsymbol{u} - \nabla\cdot\boldsymbol{\tau} + \rho(\boldsymbol{u}\cdot\nabla)\boldsymbol{u} + \nabla p &= \mathbf{0} \quad \text{in } (0,T]\times\Omega, \\ \nabla\cdot\boldsymbol{u} &= 0 \quad \text{in } (0,T]\times\Omega. \end{aligned} \tag{1}$$

In (1), $T\ [\mathrm{s}]$ is the final simulation time, $\rho = 1060\,\mathrm{kg/m^3}$ is the density of blood, and $\boldsymbol{\tau} = \boldsymbol{\tau}(\nabla\boldsymbol{u})$ is the *shear stress*, which in a generalized Newtonian fluid depends on the shear rate tensor; see (7) in Section 2.4.

The maximum diameter of the aorta is $D \approx 0.03\,\mathrm{m}$. A parabolic flow profile through a cylindrical pipe with diameter $D$ and volumetric flow rate $Q = 4.42\,\mathrm{m^3/s}$, see Table 1, bottom row, has a peak velocity of $U^* \approx 1.25\,\mathrm{m/s}$ and, with each of the viscosity models detailed in Section 2.4, a mean dynamic viscosity on the order of $\mu_{\mathrm{avg}} \approx 5\,\mathrm{mPa\cdot s}$. We can therefore very roughly estimate the peak Reynolds number of the flow as

$$\mathrm{Re} = \frac{\rho D U^*}{\mu_{\mathrm{avg}}} \approx 8000.$$

One expects a moderately turbulent flow, necessitating the use of a suitable turbulence model for the numerical simulation. As detailed in Section 2.5, we will compare the combination of each viscosity model with each of two distinct approaches to modeling turbulence.

### 2.1.1 Initial and Boundary Conditions

We complement (1) with the following initial and boundary conditions:

$$\begin{aligned} \boldsymbol{u}(0,\boldsymbol{x}) &= \mathbf{0} && \text{in } \Omega, \\ \boldsymbol{u}(t,\boldsymbol{x}) &= \boldsymbol{u}_{\mathrm{in}}(t,\boldsymbol{x}) := a(t)\boldsymbol{u}^*_{\mathrm{in}}(\boldsymbol{x}) && \text{on } [0,T]\times\Gamma_{\mathrm{in}}, \\ \boldsymbol{u}(t,\boldsymbol{x}) &= \mathbf{0} && \text{on } [0,T]\times\Gamma_{\mathrm{wall}}, \\ (\boldsymbol{\tau} - p\mathbb{I})\boldsymbol{n} &= -R_i Q_i(t)\boldsymbol{n} + \tfrac{\rho}{2}(\boldsymbol{u}\cdot\boldsymbol{n})_-\boldsymbol{u} && \text{on } [0,T]\times\Gamma_{\mathrm{out},i},\ i=1,\dots,4. \end{aligned} \tag{2}$$

That is:

- we start the simulations from a homogeneous initial velocity field, to avoid more complicated initialization procedures,

- we impose the inflow as Dirichlet boundary conditions given by a measured peak inflow profile $\boldsymbol{u}_{\mathrm{in}}^* : \Gamma_{\mathrm{in}} \to \mathbb{R}^3$ multiplied with a smooth amplitude profile $a : \mathbb{R} \to \mathbb{R}$ (plotted in Figure 2) that provides a warm-up from zero to a periodic pulse; specifically, $a(t) = 0$ for nonpositive times $t$, and $a(t + T_0)$ for all $t > t_0$, where $T_0 = 1\,\mathrm{s}$ and $t_0 = 0.01\,\mathrm{s}$,
- we impose no-slip boundary conditions on $\Gamma_{\mathrm{wall}}$, and
- we impose *directional resistive boundary conditions* on $\Gamma_i$, $i = 1, \ldots, 4$.

In the directional resistive boundary conditions $(2)_4$, the additional term $\frac{\rho}{2}(\boldsymbol{u} \cdot \boldsymbol{n})_- \boldsymbol{u}$ provides stabilization against oscillations that can otherwise arise in the presence of backflow. This approach was introduced in [10, 11], emerging as a natural way of controlling energy estimates on $\nabla \boldsymbol{u}$. The other term on the right-hand side is the product of a constant *vascular resistance* $R_i$ $\left[\mathrm{Pa{\cdot}s}/\mathrm{m}^3\right]$ and the volumetric outflow

$$Q_i(t) = \int_{\Gamma_i} \big(\boldsymbol{u}(t, \cdot) \cdot \boldsymbol{n}\big)\, \mathrm{d}\mu_{\Gamma_i}$$

through the same outlet, representing a simple lumped model of the downstream circulation beyond each outlet.

Table 1: Estimated flow rates and corresponding fraction of the inlet flow (absolute value) for each outlet (see also Figure 1, left) used in the simulations.

| Boundary | Flow $Q_i^*$ [m$^3$/s] | Flow fraction $\mathrm{out}_i$ |
|---|---|---|
| $\Gamma_{\mathrm{out},1}$ (brachiocephalic artery) | $7.43 \cdot 10^{-5}$ | 16.81 % |
| $\Gamma_{\mathrm{out},2}$ (left common carotid artery) | $3.80 \cdot 10^{-5}$ | 8.60 % |
| $\Gamma_{\mathrm{out},3}$ (left common subclavian artery) | $3.63 \cdot 10^{-5}$ | 8.21 % |
| $\Gamma_{\mathrm{out},4}$ (descending aorta) | $2.93 \cdot 10^{-4}$ | 66.38 % |
| Inlet | $4.42 \cdot 10^{-4}$ | 100.00 % |

The resistances at each outlet, listed in Table 2, are tuned so as to closely match[1] the peak outflow rates listed in Table 1 and achieve a total downstream resistance of $115\,\mathrm{MPa{\cdot}s}/\mathrm{m}^3$; see [4] for further details. This total resistance was chosen close to the middle of the clinical reference range for the systemic vascular resistance, a zero-dimensional lumped model commonly used to express the overall relationship between blood flow rate and pressure in the systemic circulation, e.g., see [12]. As shown in [4], the choice of the downstream resistance, within a range of clinically reasonable values, has negligible impact on diagnostically relevant flow statistics.

Table 2: Resistances $\left[\mathrm{MPa{\cdot}s}/\mathrm{m}^3\right]$ at each outlet for the considered turbulence models.

| Turbulence model | $R_1$ | $R_2$ | $R_3$ | $R_4$ |
|---|---|---|---|---|
| $\boldsymbol{\sigma}$-model, $C_\sigma = 1.35$ | 709.05 | 1335.9 | 1358.1 | 172.40 |
| RB-VMS, $\mathrm{P}_1/\mathrm{P}_1$ elements, fine mesh | 717.03 | 1333.3 | 1326.3 | 172.50 |

[1] Specifically, the relative error in a constant-inflow simulation with constant (Newtonian) viscosity $\mu = 3.5\,\mathrm{mPa \cdot s}$ and a given turbulence model, averaged over a quarter-second of simulated time after a quarter-second of warmup, was below $10^{-3}$ at each outlet.

## 2.2 Dimensionless Equations

Dividing (1) and (2) by $\rho$ and using velocity and distance scales $U = 1\,\mathrm{m/s}$ and $L = 1\,\mathrm{m}$, we arrive at the fully dimensionless form

$$\begin{aligned} \partial_t \tilde{\boldsymbol{u}} - \nabla \cdot \tilde{\boldsymbol{\tau}} + (\tilde{\boldsymbol{u}} \cdot \nabla)\tilde{\boldsymbol{u}} + \nabla \tilde{p} &= \boldsymbol{0} \quad \text{in } (0,T] \times \Omega, \\ \nabla \cdot \tilde{\boldsymbol{u}} &= 0 \quad \text{in } (0,T] \times \Omega, \end{aligned} \tag{3}$$

with boundary conditions

$$\begin{aligned} \tilde{\boldsymbol{u}}(0,\boldsymbol{x}) &= \boldsymbol{0} && \text{in } \Omega, \\ \tilde{\boldsymbol{u}}(t,\boldsymbol{x}) &= \tilde{\boldsymbol{u}}_{\mathrm{in}}(t,\boldsymbol{x}) := a(t)\tilde{\boldsymbol{u}}^*_{\mathrm{in}}(\boldsymbol{x}) && \text{on } [0,T] \times \Gamma_{\mathrm{in}}, \\ \tilde{\boldsymbol{u}}(t,\boldsymbol{x}) &= \boldsymbol{0} && \text{on } [0,T] \times \Gamma_{\mathrm{wall}}, \\ (\tilde{\boldsymbol{\tau}} - \tilde{p}\mathbb{I})\boldsymbol{n} &= -\tilde{R}_i \tilde{Q}_i(t)\boldsymbol{n} + \tfrac{1}{2}(\tilde{\boldsymbol{u}} \cdot \boldsymbol{n})_- \tilde{\boldsymbol{u}} && \text{on } [0,T] \times \Gamma_{\mathrm{out},i},\ i = 1,\dots,4. \end{aligned} \tag{4}$$

Here $\tilde{\boldsymbol{u}} = \frac{1}{U}\boldsymbol{u}$, $\tilde{\boldsymbol{\tau}} = \frac{1}{\rho U^2}\boldsymbol{\tau}$, $\tilde{p} = \frac{1}{\rho U^2}p$, $\tilde{R}_i = \frac{UL^2}{\rho}R_i$, $\tilde{Q}_i = \frac{1}{UL^2}Q_i$ denote the dimensionless quantities. We will slightly abuse notation by not continuing to mark these distinctions on the dimensionless discretized velocities and pressures $\boldsymbol{u}_h$ and $p_h$.

## 2.3 Spatial and Temporal Discretizations

We discretize (3) in space using a finite element method. Let $\mathcal{T}_h \in \{\mathcal{T}, \mathcal{T}'\}$ be a regular tetrahedral mesh representing $\Omega$. Let $\boldsymbol{V}_h \subset \mathrm{C}(\Omega, \mathbb{R}^3)$ and $Q_h \subset \mathrm{C}(\Omega, \mathbb{R})$ denote continuous piecewise polynomial spaces on $\mathcal{T}_h$, and let

$$\boldsymbol{V}_{h,0} = \{\boldsymbol{v}_h \in \boldsymbol{V}_h : \boldsymbol{v}_h \equiv \boldsymbol{0} \text{ on } \Gamma_{\mathrm{in}} \cup \Gamma_{\mathrm{wall}}\}$$

be the subspace of $\boldsymbol{V}_h$ with homogeneous Dirichlet boundary conditions on the wall and the inlet boundary.

Consider the nonlinear form

$$\begin{aligned} \mathrm{Gal}\Big((\boldsymbol{u}_h, p_h), (\boldsymbol{v}_h, q_h)\Big) &= a(\boldsymbol{u}_h, \boldsymbol{v}_h) + b(\boldsymbol{u}_h; \boldsymbol{u}_h, \boldsymbol{v}_h) \\ &\quad -(\nabla \cdot \boldsymbol{v}_h, p_h) + (\nabla \cdot \boldsymbol{u}_h, q_h) - f(\boldsymbol{u}_h, \boldsymbol{v}_h) \end{aligned}$$

with the generally nonlinear viscosity form

$$a(\boldsymbol{u}_h, \boldsymbol{v}_h) := (\tilde{\boldsymbol{\tau}}(\nabla \boldsymbol{u}_h), \mathbb{D}(\boldsymbol{v}_h)) \quad \text{with} \quad \mathbb{D}(\boldsymbol{v}_h) = \frac{1}{2}\left(\nabla \boldsymbol{v}_h + (\nabla \boldsymbol{v}_h)^T\right),$$

the trilinear convective form

$$b(\boldsymbol{u}_h; \boldsymbol{v}_h, \boldsymbol{w}_h) := \big((\boldsymbol{u}_h \cdot \nabla)\boldsymbol{v}_h, \boldsymbol{w}_h\big),$$

and the nonlinear boundary form

$$f(\boldsymbol{u}_h, \boldsymbol{v}_h) := \sum_{i=1}^{4} \left( P_i(\boldsymbol{u}_h)\boldsymbol{n} + \frac{1}{2}(\boldsymbol{u}_h \cdot \boldsymbol{n})_- \boldsymbol{u}_h, \boldsymbol{v}_h \right)_{\Gamma_{\mathrm{out},i}}$$

for the directional resistive boundary conditions.

The continuous-in-time Galerkin discrete formulation of (3) reads: Find $(\boldsymbol{u}_h, p_h) : [0,T] \to \boldsymbol{V}_h \times Q_h$ such that $\boldsymbol{u}_h \equiv \boldsymbol{0}$ on $[0,T] \times \Gamma_{\text{wall}}$, $\boldsymbol{u}_h$ satisfies $(4)_1$, and

$$(\partial_t \boldsymbol{u}_h, \boldsymbol{v}_h) + \mathrm{Gal}\Big((\boldsymbol{u}_h, p_h), (\boldsymbol{v}_h, q_h)\Big) = 0 \tag{5}$$

for all $t \in (0,T)$ and for all $(\boldsymbol{v}_h, q_h) \in \boldsymbol{V}_{h,0} \times Q_h$.

To solve (5), or its modifications detailed in Section 2.5, we employ a BDF-2 scheme, an A-stable second order method. This scheme has the advantage of requiring residuals of only the current time step. However, it does require the solution at two previous time steps, so the first time iteration is performed using the backward Euler method.

At each time step, a nonlinear problem in the velocity and pressure must be solved. This is achieved by Picard iteration: the convective form $b$, the boundary form $f$, and the viscosity form $a$ are linearized using the velocity field $\hat{\boldsymbol{u}}_h$ computed by the previous step of the iteration:

$$\begin{aligned} \widehat{\mathrm{Gal}}\left((\boldsymbol{u}_h, p_h), (\boldsymbol{v}_h, q_h)\right) &= \hat{a}(\boldsymbol{u}_h, \boldsymbol{v}_h) + b(\hat{\boldsymbol{u}}_h; \boldsymbol{u}_h, \boldsymbol{v}_h) \\ &\quad -(\nabla \cdot \boldsymbol{v}_h, p_h) + (\nabla \cdot \boldsymbol{u}_h, q_h) - f(\hat{\boldsymbol{u}}_h, \boldsymbol{v}_h), \end{aligned} \tag{6}$$

where the solution $(\boldsymbol{u}_h, p_h)$ denotes the next iterate and $\hat{a}$ is a linearized version of the viscosity form $a$ in which the effective viscosity is computed from $\hat{\boldsymbol{u}}_h$ as in (8) below. We provide initial guesses $(\hat{\boldsymbol{u}}_h, \hat{p}_h)$ for the first iteration by linearly extrapolating from the solutions computed at the two preceding time steps.

## 2.4 Viscosity Modeling

Each of the models below is implemented as an *isotropic generalized Newtonian fluid* - that is, the shear stress takes the form

$$\boldsymbol{\tau} = \mu_{\text{eff}}(\dot{\gamma})\dot{\boldsymbol{\gamma}} \quad [\mathrm{Pa}], \tag{7}$$

where

$$\dot{\boldsymbol{\gamma}} = 2\mathbb{D}(\boldsymbol{u}) = \nabla \boldsymbol{u} + (\nabla \boldsymbol{u})^T \quad [\mathrm{s}^{-1}]$$

is the shear rate tensor, and $\mu_{\text{eff}}(\dot{\gamma})$ $[\mathrm{Pa} \cdot \mathrm{s}]$ is a dynamic viscosity that depends on the scalar shear rate

$$\dot{\gamma} = \sqrt{\frac{1}{2}\|\dot{\boldsymbol{\gamma}}\|_F^2} \quad [\mathrm{s}^{-1}]\,.$$

Taking the dimensionless effective viscosity $\nu_{\text{eff}} = \frac{U}{L\rho}\mu_{\text{eff}}$ and the discrete velocity's shear rate

$$\dot{\gamma}_h = \dot{\gamma}_h(\boldsymbol{u}_h) = \sqrt{2\|\mathbb{D}(\boldsymbol{u}_h)\|_F^2},$$

and shear stress

$$\boldsymbol{\tau}_h = 2\nu_{\text{eff}}(\dot{\gamma}_h)\mathbb{D}(\boldsymbol{u}_h),$$

we can specify the linearized viscosity form in (6):

$$\hat{a}(\boldsymbol{u}_h, \boldsymbol{v}_h) := \left(2\nu_{\text{eff}}\left(\dot{\gamma}_h(\hat{\boldsymbol{u}}_h)\right)\mathbb{D}(\boldsymbol{u}_h), \mathbb{D}(\boldsymbol{v}_h)\right). \tag{8}$$

Each model has a number of parameters describing the scale and behavior of the fluid's viscosity as shear rate changes, which have been variously fitted to blood viscosity measurements.

### 2.4.1 Newtonian Fluid

A Newtonian fluid has constant isotropic viscosity, that is

$$\mu_{\text{eff}}(\dot{\gamma}) \equiv \mu^*,$$

i.e., independent on the value of $\dot{\gamma}$. In our Newtonian simulations we use the value

$$\mu^* = 3.5\,\text{mPa}\cdot\text{s},$$

which is a common choice for Newtonian simulations in large blood vessels (see, e.g. [4, 13, 14, 15]), and it is close to the viscosity at large shear rates as computed by each non-Newtonian model below.

The simulation results obtained using a Newtonian flow model will be labeled (**NEWT**).

### 2.4.2 Power-law Fluid

The simplest commonly used non-Newtonian fluid model assumes a *power-law* relationship. Rheology experiments in the early 20th century, e.g., see [16], yielded the observation that, in fluids such as starch or protein suspensions, the logarithms of shear rate and shear stress are (almost) linearly related across much of the measurable range, motivating the modeling of viscosity by a power law relation

$$\mu_{\text{eff}}(\dot{\gamma}) = k\dot{\gamma}^{n-1} \tag{9}$$

for $\dot{\gamma} > 0$, with the dimensionless *flow behavior index* $n \in \mathbb{R}$, and the *flow consistency index* $k$ $[\text{Pa}\cdot\text{s}^{\text{n}}]$. Notice that for a shear-thinning fluid ($n < 1$) the effective viscosity becomes singular near zero shear rate and vanishes as shear rate increases. In our simulations, we regularize by cutting off the viscosity:

$$\mu_{\text{eff}}(\dot{\gamma}) = \begin{cases} \max\{\min\{k\dot{\gamma}^{n-1}, \mu_{\max}\}, \mu_{\min}\} & \text{if } \dot{\gamma} > 0, \\ \mu_{\max} & \text{if } \dot{\gamma} = 0. \end{cases} \tag{10}$$

Here $\mu_{\min}, \mu_{\max}$ $[\text{Pa}\cdot\text{s}]$ are the smallest and largest viscosity the simulated fluid is allowed to attain.

We use the following values in our simulations:

$$\begin{aligned} n &= 0.7, & k &= 0.02\,\text{Pa}\cdot\text{s}^{0.7}, \\ \mu_{\min} &= 2.2\,\text{mPa}\cdot\text{s}, & \mu_{\max} &= 1\,\text{kPa}\cdot\text{s}. \end{aligned}$$

The values for $k$ and $n$ are taken following [5]. The value of $\mu_{\min}$ is taken from the smallest limiting viscosity of blood we have encountered in the literature (see Section 2.4.3); $\mu_{\max}$ is chosen to lie at the extreme of computational feasibility.

The results of our regularized power-law simulations will be labeled (**POW**).

### 2.4.3 Carreau–Yasuda Fluid

In the Carreau–Yasuda model [17] the fluid viscosity obeys the equation

$$\mu_{\text{eff}}(\dot{\gamma}) = \mu_\infty + (\mu_0 - \mu_\infty)(1 + (\lambda\dot{\gamma})^a)^{\frac{n-1}{a}} \tag{11}$$

with dimensionless power indices $n$ and $a$, relaxation time $\lambda$ $[\mathrm{s}]$, and limiting viscosities $\mu_\infty, \mu_0$ $[\mathrm{Pa}\cdot\mathrm{s}]$. The model proposed in [17] is a generalization of the earlier Carreau B model [18], which corresponds to $a = 2$ in (11).

The flexibility of this model in describing varying flow behaviors makes it a popular choice for modeling blood. As the concrete realizations in the literature vary widely, we use three sets of parameters derived from different measurements:

(**CY-0**): Following [6]:

$$\begin{aligned} n &= 0.22, & a &= 1.25, & \lambda &= 1.902\,\mathrm{s}, \\ \mu_\infty &= 3.45\,\mathrm{mPa}\cdot\mathrm{s}, & \mu_0 &= 56\,\mathrm{mPa}\cdot\mathrm{s}. \end{aligned}$$

(**CY-1**): Following [7]:

$$\begin{aligned} n &= 0.392, & a &= 0.644, & \lambda &= 0.11\,\mathrm{s}, \\ \mu_\infty &= 2.2\,\mathrm{mPa}\cdot\mathrm{s}, & \mu_0 &= 22\,\mathrm{mPa}\cdot\mathrm{s}. \end{aligned}$$

(**CY-2**): Following [8]:

$$\begin{aligned} n &= 0.2128, & a &= 0.64, & \lambda &= 8.2\,\mathrm{s}, \\ \mu_\infty &= 3.5\,\mathrm{mPa}\cdot\mathrm{s}, & \mu_0 &= 160\,\mathrm{mPa}\cdot\mathrm{s}. \end{aligned}$$

#### 2.4.4 Casson Fluid

The Casson fluid model, originally introduced in [19] in the context of modeling printing ink, was soon applied to blood flow, e.g., in [20], though with particular regard to smaller blood vessels.

The Casson fluid model is notable in that it has nonzero *yield stress*:

$$\mu_{\mathrm{eff}}(\dot\gamma) = \left(\sqrt{\frac{\tau_0}{\dot\gamma}} + \sqrt{\mu_\infty}\right)^2 \tag{12}$$

for $\dot\gamma > 0$, so that

$$\lim_{\dot\gamma\to 0} \mu_{\mathrm{eff}}(\dot\gamma)\dot\gamma = \tau_0.$$

Here, $\tau_0$ $[\mathrm{Pa}]$ is the yield stress and $\mu_\infty$ $[\mathrm{Pa}\cdot\mathrm{s}]$ is the limiting viscosity at infinite shear rate. Since this formula again yields a singular value near zero shear rate, we regularize it by imposing an upper limit, i.e.

$$\mu_{\mathrm{eff}}(\dot\gamma) = \begin{cases} \min\left\{\left(\sqrt{\frac{\tau_0}{\dot\gamma}} + \sqrt{\mu_\infty}\right)^2, \mu_{\max}\right\} & \text{if } \dot\gamma > 0, \\ \mu_{\max} & \text{if } \dot\gamma = 0, \end{cases} \tag{13}$$

with a maximum viscosity $\mu_{\max}$ $[\mathrm{Pa}\cdot\mathrm{s}]$.

Following [9] for the yield stress and limiting viscosity and using the same maximum viscosity as in Section 2.4.2, we take

$$\tau_0 = 4\,\mathrm{mPa}, \quad \mu_\infty = 3.5\,\mathrm{mPa}\cdot\mathrm{s}, \quad \mu_{\max} = 1\,\mathrm{kPa}\cdot\mathrm{s}\,.$$

The simulation results for the Casson model are labelled (**CASS**).

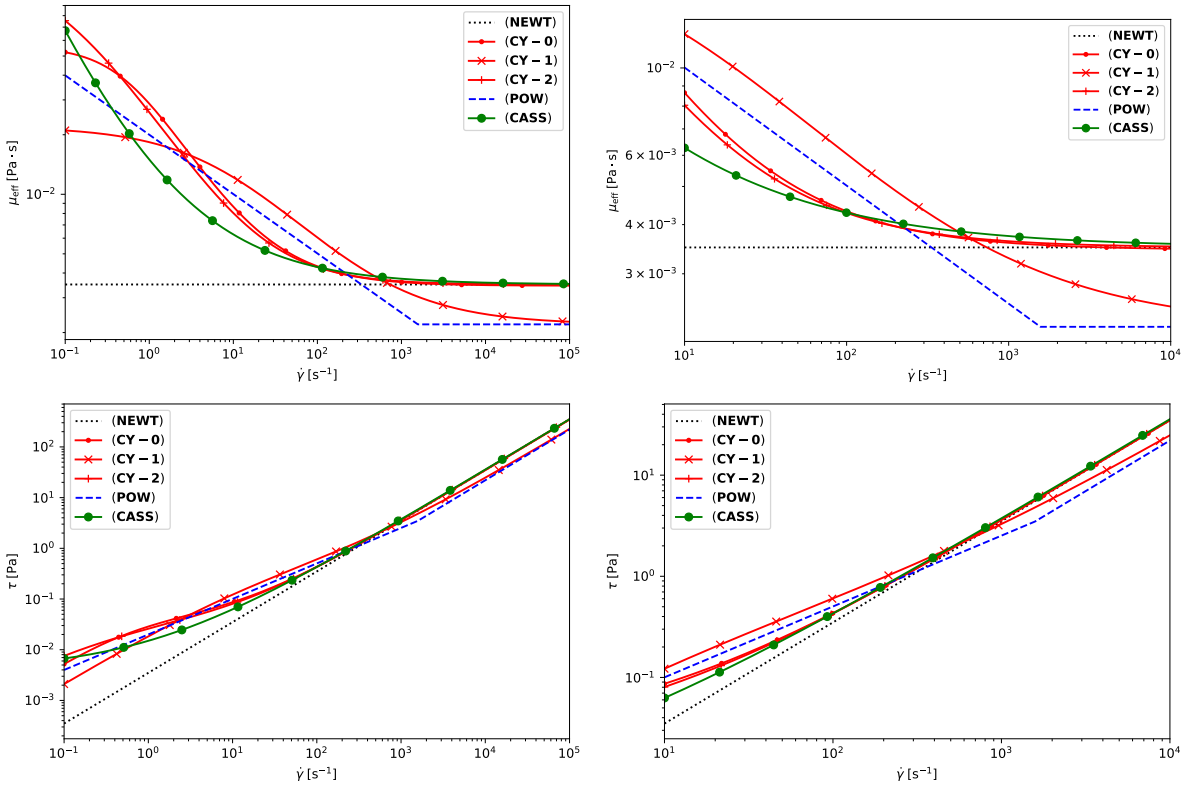


Figure 3: Dependency of the viscosity models on the shear rate. Upper left: Effective viscosity over a large shear rate range. Upper right: Effective viscosity over a smaller range of shear rates most relevant during simulations. Lower left: Effective shear stress over a large range. Lower right: Effective shear stress over a smaller range.

### 2.4.5 Dependency of the Viscosity Models on the Shear Rate

Figure 3 compares the effective viscosities and shear stresses given by each model over a representative range of shear rates. The right-hand graphs show the range of shear rates most relevant during our simulations: very slow shear rates below $10\,\mathrm{s}^{-1}$ appear in regions of significant extent only briefly during the dissipative period at the end of diastole, and very rapid shear rates above $10^4\,\mathrm{s}^{-1}$ appear only in small regions around inflection points such as the inner edge of the coarctation.

It is clear that (**CY-0**), (**CY-2**), and (**CASS**) result in fairly similar behaviors in this range, whereas (**CY-1**) and (**POW**) deviate considerably. Indeed, the mid-range behavior of (**CY-1**) clearly resembles a power-law fluid with behavior index close to that of (**POW**) at a slightly different scale.

## 2.5 Turbulence Modeling

The numerical studies concerning the impact of turbulence modeling in the context of a Newtonian blood flow model presented in [4] indicate that, based on selected quantities of interest, turbulence models can be classified in two main groups, depending on the amount of numerical viscosity introduced. One representative of each group was chosen for performing the numerical studies presented in Section 4, in order to compare the impact of viscosity modeling to that of turbulence modeling. Both these models belong, in the broadest sense, to the *large eddy simulation* (LES) family of models in that

they seek to reproduce flow behavior at feasibly resolvable *spatial* scales by modeling its interaction with fine-scale flow structures without explicitly computing these.

Our two models of choice nevertheless represent two different approaches to turbulence modeling: the $\boldsymbol{\sigma}$-model (Section 2.5.1) proceeds from the traditional LES notion of separating scales by applying a convolutional spatial low-pass filter to the continuous equation (3) and modeling the *subgrid-scale stress tensor* to account for interactions between fine and coarse velocity scales. The residual-based variational multiscale method (Section 2.5.2) begins instead from the variational formulation (5) and separates the scales explicitly using the finite element discretization. The numerical studies in [4] showed that the $\boldsymbol{\sigma}$-model belongs to a group of turbulence models that introduce comparably little numerical viscosity, whereas the residual-based variational multiscale method introduces notably more numerical viscosity.

### 2.5.1 The $\sigma$-model

The $\boldsymbol{\sigma}$-model, introduced in [21], is a classical eddy viscosity model, adding to the left-hand side of (5) an artificial viscosity term representing the loss of energy from the resolved scales to the subgrid scales:

$$(\partial_t \boldsymbol{u}_h, \boldsymbol{v}_h) + \mathrm{Gal}\Big((\boldsymbol{u}_h, p_h), (\boldsymbol{v}_h, q_h)\Big) + 2\big(\nu_t(\boldsymbol{u}_h)\mathbb{D}(\boldsymbol{u}_h), \mathbb{D}(\boldsymbol{v}_h)\big) = 0$$

with a (pointwise) eddy viscosity $\nu_t(\boldsymbol{u}_h)$, which estimates coarse-fine interactions by the behavior of the resolved velocity field.

In [21], it is postulated based on concerns of practicality and on data from high-fidelity simulations and experiments that the eddy viscosity $\nu_t$ must

- be computed locally from the gradient of the resolved velocity field and scale with it,
- scale with the cube of the distance from solid boundaries in simple shear flow scenarios,
- vanish in regions of less than three-dimensional flow behavior, and
- vanish in regions of axisymmetric expansion or contraction.

Combining these key requirements with the idea of computing the eddy viscosity from the velocity gradient's singular values $\sigma_1 \geq \sigma_2 \geq \sigma_3 \geq 0$, one arrives at

$$\nu_t(\boldsymbol{u}_h) = (C_\sigma \delta)^2 \frac{\sigma_3(\sigma_1 - \sigma_2)(\sigma_2 - \sigma_3)}{\sigma_1^2}.$$

Here, $\delta$ is a local length scale, in our case, twice the shortest edge length of the local tetrahedral cell, and $C_\sigma$ is a scaling parameter. Following [21], we use the value $C_\sigma = 1.35$.

We use the $\boldsymbol{\sigma}$-model with Taylor-Hood $(\mathrm{P}_2/\mathrm{P}_1)$ elements on the base mesh $\mathcal{T}$; for the purpose of the Picard iteration scheme, $\nu_t$ is computed from the previous iterate $\hat{\boldsymbol{u}}_h$.

### 2.5.2 RB-VMS Model

In [22], a residual-based variational multiscale (RB-VMS) method was developed. A (two-scale) variational multiscale method separates the solution $(\tilde{\boldsymbol{u}}, \tilde{p})$ of (3) into two scales by use of the finite element discretization:

$$(\tilde{\boldsymbol{u}}, \tilde{p}) = (\boldsymbol{u}_h, p_h) + (\boldsymbol{u}', p').$$

The coarse solution $(\boldsymbol{u}_h, p_h)$ is then assumed to be uniquely determined by some projection of $(\tilde{\boldsymbol{u}}, \tilde{p})$ onto $\boldsymbol{V}_h \times Q_h$, and from this starting point a model for the fine scales $(\boldsymbol{u}', p')$ and their interaction with $(\boldsymbol{u}_h, p_h)$ is developed.

In the case of [22], this involves representing the fine scales by a perturbation series in the norm of the residuals and approximating the fine-scale Green's operator by using just the first term of this series, see also [23] for details. The result, for Newtonian flow ($\boldsymbol{\tau}_h = 2\nu\mathbb{D}(\boldsymbol{u}_h)$ with a constant dimensionless viscosity $\nu$), is:

$$\begin{aligned}\boldsymbol{u}' &\approx -\tau_m \boldsymbol{r}_m(\boldsymbol{u}_h, p_h) = -\tau_m \left(\partial_t \boldsymbol{u}_h + (\boldsymbol{u}_h \cdot \nabla)\boldsymbol{u}_h + \nabla p_h - \nu\Delta\boldsymbol{u}_h\right), \\ p' &\approx -\tau_c r_c(\boldsymbol{u}_h) = -\tau_c(\nabla \cdot \boldsymbol{u}_h),\end{aligned}$$

with stabilization parameters $\tau_m$ and $\tau_c$. A variational formulation is then derived by adding the missing coarse-fine, fine-coarse and fine-fine terms to (5). Note, however, that:

(i) the second derivatives of $\boldsymbol{u}_h$ are generally not well-defined globally. This may be dealt with by using only values in the interior of each cells or by applying a projection,

(ii) in our case of a generalized Newtonian fluid with a nonconstant dimensionless viscosity $\nu_{\mathrm{eff}}$ depending on $\mathbb{D}(\boldsymbol{u}_h)$, the divergence of $\boldsymbol{\tau}_h$ includes an additional term with first derivatives of $\nu_{\mathrm{eff}}$.

We applied the RB-VMS model in combination with continuous piecewise linear ($\mathrm{P}_1/\mathrm{P}_1$) elements. As $\nu_{\mathrm{eff}}$ is a function of $\dot{\gamma}_h$, which is a function of first derivatives of the coarse velocity $\boldsymbol{u}_h$, all terms of

$$\nabla \cdot \boldsymbol{\tau}_h = \nu_{\mathrm{eff}}(\dot{\gamma}_h)\left(\Delta\boldsymbol{u}_h + \nabla\left(\nabla \cdot \boldsymbol{u}_h\right)\right) + 2{\nu_{\mathrm{eff}}}'(\dot{\gamma}_h)\nabla\dot{\gamma}_h\mathbb{D}(\boldsymbol{u}_h)$$

involve second derivatives of $\boldsymbol{u}_h$. Thus, if $\boldsymbol{u}_h$ is piecewise linear, $\nabla\cdot\boldsymbol{\tau}_h$ vanishes when using pointwise derivatives in the interior of mesh cells.

In our case, therefore, the momentum residual takes the form

$$\boldsymbol{r}_m(\boldsymbol{u}_h, p_h) = \partial_t\boldsymbol{u}_h + (\boldsymbol{u}_h \cdot \nabla)\boldsymbol{u}_h + \nabla p_h.$$

Using integration by parts to avoid derivatives of the residuals and making some additional simplifying assumptions, see also [24, Rem 8.224], we obtain the following variational problem: find $(\boldsymbol{u}_h, p_h) : [0,T] \to \boldsymbol{V}_h \times Q_h$ such that

$$\begin{aligned}&(\partial_t\boldsymbol{u}_h, \boldsymbol{v}_h) + \mathrm{Gal}\left((\boldsymbol{u}_h, p_h), (\boldsymbol{v}_h, q_h)\right) \\ &\qquad + \tau_m\left(\boldsymbol{r}_m(\boldsymbol{u}_h, p_h), (\boldsymbol{u}_h \cdot \nabla)\boldsymbol{v}_h\right) + \tau_m\left(\boldsymbol{r}_m(\boldsymbol{u}_h, p_h), \nabla q_h\right) \\ &\qquad + \tau_c\left(r_c(\boldsymbol{u}_h), \nabla \cdot \boldsymbol{v}_h\right) + \tau_m\left(\boldsymbol{r}_m(\boldsymbol{u}_h, p_h), (\nabla\boldsymbol{v}_h)^T\boldsymbol{u}_h\right) \\ &\qquad - \tau_m^2\left(\boldsymbol{r}_m(\boldsymbol{u}_h, p_h) \otimes \boldsymbol{r}_m(\boldsymbol{u}_h, p_h), \nabla\boldsymbol{v}_h\right) = 0\end{aligned} \tag{14}$$

at all times $t \in (0,T]$ and for all $\boldsymbol{v}_h \in \boldsymbol{V}_{h,0}$, $q_h \in Q_h$.

In (14), the form $\mathrm{Gal}(\cdot,\cdot)$ denotes the terms resulting from the Galerkin discretization of (3) as in (5). Most of the remaining terms result from the interactions of the coarse and fine scales; the last term represents fine-fine interactions. As one of the terms couples the momentum residual (which includes the pressure gradient) with pressure test functions, the resulting systems will include a nonsingular pressure-pressure block. Consequently, the RB-VMS model does not require inf-sup stable velocity-pressure pairs.

With the exception of the grad-div term $\tau_c\left(r_c(\boldsymbol{u}_h), \nabla \cdot \boldsymbol{v}_h\right)$, every additional term in (14) is necessarily at least quadratic in $\boldsymbol{u}_h$, and the final term is quadratic in $p_h$. Additionally, the stabilization parameters may depend on the solution. There are therefore various possible approaches for linearizing the

problem for applying a Picard iteration. Where the stabilization parameters depend on the solution, they are computed from the previous iterate; the momentum residual $\boldsymbol{r}_m$ is linearized as usual by taking the previous iterate as the convection field:

$$\hat{\boldsymbol{r}}_m(\boldsymbol{u}_h, p_h) = \partial_t \boldsymbol{u}_h + (\hat{\boldsymbol{u}}_h \cdot \nabla)\boldsymbol{u}_h + \nabla p_h.$$

With some additional decisions, we obtain the following linearized problem:

$$\begin{aligned}(\partial_t \boldsymbol{u}_h, \boldsymbol{v}_h) &+ \widehat{\mathrm{Gal}}\left((\boldsymbol{u}_h, p_h), (\boldsymbol{v}_h, q_h)\right) \\ &+ \tau_m\left(\hat{\boldsymbol{r}}_m(\boldsymbol{u}_h, p_h), (\hat{\boldsymbol{u}}_h \cdot \nabla)\boldsymbol{v}_h\right) + \tau_m\left(\hat{\boldsymbol{r}}_m(\boldsymbol{u}_h, p_h), \nabla q_h\right) \\ &+ \tau_c\left(r_c(\boldsymbol{u}_h), \nabla \cdot \boldsymbol{v}_h\right) + \tau_m\left(\hat{\boldsymbol{r}}_m(\boldsymbol{u}_h, p_h), (\nabla \boldsymbol{v}_h)^T \hat{\boldsymbol{u}}_h\right) \\ &- \tau_m^2\left(\hat{\boldsymbol{r}}_m(\hat{\boldsymbol{u}}_h, \hat{p}_h) \otimes \hat{\boldsymbol{r}}_m(\boldsymbol{u}_h, p_h), \nabla \boldsymbol{v}_h\right) = 0,\end{aligned} \tag{15}$$

where $\widehat{\mathrm{Gal}}(\cdot,\cdot)$ denotes the linearization of the Galerkin terms, as in (6). Notice that the time derivative of the velocity appears in the momentum residual $\boldsymbol{r}_m$ (and its linearization $\hat{\boldsymbol{r}}_m$). We shift the terms involving $\partial_t \boldsymbol{u}_h$ to the time discretization's modified mass matrix; $\partial_t \hat{\boldsymbol{u}}_h$ is approximated as the difference quotient

$$\partial_t \hat{\boldsymbol{u}}_h \approx \frac{1}{\Delta t}\left(\hat{\boldsymbol{u}}_h - \boldsymbol{u}_{h,\mathrm{prev}}\right),$$

where $\boldsymbol{u}_{h,\mathrm{prev}}$ is the previous time step's velocity.

Concerning the choice of the stabilization parameters $\tau_m$, $\tau_c$, we again follow [22, Eq.(63), (64)], where the following values are suggested for equal-order pairs (based on asymptotic scaling arguments):

$$\begin{aligned}\tau_m(K, \boldsymbol{u}_h) &= \left(\frac{4}{\Delta t^2} + \boldsymbol{u}_h \cdot \boldsymbol{G}\boldsymbol{u}_h + C_I \nu^2 (\boldsymbol{G} : \boldsymbol{G})\right)^{-\frac{1}{2}}, \\ \tau_c(K, \boldsymbol{u}_h) &= \frac{1}{\tau_m(K, \boldsymbol{u}_h)|\boldsymbol{g}|^2}.\end{aligned} \tag{16}$$

In (16), $K$ denotes the local cell of the tetrahedral finite element mesh, $\boldsymbol{G} = \boldsymbol{G}(K) = (\nabla \boldsymbol{F}_K^{-1})^T \nabla \boldsymbol{F}_K^{-1}$ and $\boldsymbol{g} = \boldsymbol{G}(K) = \mathbf{1}^T \nabla \boldsymbol{F}_K^{-1}$ are derived from the local reference transformation $\boldsymbol{F}_K^{-1} : K \to \hat{K}$ from $K$ to the reference tetrahedron $\hat{K} = \mathrm{conv}\,(\mathbf{0}, \boldsymbol{e}_1, \boldsymbol{e}_2, \boldsymbol{e}_3)$, and $C_I$ is the constant of an element-wise inverse estimate. The concrete value of the constant in the inverse estimate is not of importance for our simulations because the term with $C_I$ possesses only very little impact since $\nu^2$ is very small. We used $C_I = 1$ and a dimensionless viscosity corresponding to $3.5\,\mathrm{mPa} \cdot \mathrm{s}$.

We apply the piecewise linear RB-VMS model on the uniformly refined mesh $\mathcal{T}'$, such that the velocity space has the same dimension as the corresponding $\mathrm{P}_2$ space on $\mathcal{T}$, compare Table 3.

# 3 Quantities of Interest

In this section we will introduce a number of flow statistics used in assessing the severity of various cardiovascular conditions.

## 3.1 Pressure Difference

Pressure differences across narrowed portions of major blood vessels (as in coarctation of the aorta) are an important criterion for judging the severity of the condition. Given two planar cross-sections

$S, S' \subset \Omega$, both approximately orthogonal to the main direction of flow, we will monitor the difference between averaged pressures on the two cross-sections:

$$P_{S'} - P_S = \frac{1}{|S'|}\int_{S'} p(t,\boldsymbol{x})\,\mathrm{d}\mu_{S'}(\boldsymbol{x}) - \frac{1}{|S|}\int_S p(t,\boldsymbol{x})\,\mathrm{d}\mu_S(\boldsymbol{x})\ [\mathrm{Pa}].$$

## 3.2 Maximum Velocity

Similarly, high peak flow velocities within the narrowed region and delayed decay of diastolic velocity downstream of it may also be indicative of the seriousness of the coarctation. We are interested in the maximum velocity magnitude

$$\max_{\boldsymbol{x}\in X} |\boldsymbol{u}(t,\boldsymbol{x})|\ [\mathrm{m/s}]$$

over a region $X \subset \Omega$, which may be a planar cross-section or a region enclosed between two planar cross-sections, and the minimum and maximum normal velocity

$$\min_{\boldsymbol{x}\in S}\big(\boldsymbol{u}(t,\boldsymbol{x})\cdot\boldsymbol{n}_S\big),\ \max_{\boldsymbol{x}\in S}\big(\boldsymbol{u}(t,\boldsymbol{x})\cdot\boldsymbol{n}_S\big)\ [\mathrm{m/s}]$$

through a planar cross-section $S \subset \Omega$ with forward normal $\boldsymbol{n}_S$.

## 3.3 Secondary Flow Degree (SFD)

The secondary flow degree (SFD) is a dimensionless quantity describing the "swirliness" of the flow through a planar cross-section $S \subset \Omega$ with normal $\boldsymbol{n}_S$. It is defined as the ratio between the total tangential (in-plane) velocity magnitude and the total normal (through-plane) velocity:

$$\mathrm{SFD}_S(t) := \frac{\int_S |\boldsymbol{u}(t,\boldsymbol{x}) - \big(\boldsymbol{u}(t,\boldsymbol{x})\cdot\boldsymbol{n}_S\big)\boldsymbol{n}_S|\mathrm{d}\mu_S(\boldsymbol{x})}{\int_S |\boldsymbol{u}(t,\boldsymbol{x})\cdot\boldsymbol{n}_S|\mathrm{d}\mu_S(\boldsymbol{x})}.$$

## 3.4 Normalized Flow Displacement (NFD)

The normalized flow displacement describes the eccentricity of the flow through a planar cross-section of the domain. Given $S \subset \Omega$ with normal $\boldsymbol{n}_S$ and defining the normal flow moment through $S$ as

$$\boldsymbol{x}_{\mathrm{n}}\big(\boldsymbol{u}(t,\cdot),S\big) := \frac{\int_S |\boldsymbol{u}(t,\boldsymbol{x})\cdot\boldsymbol{n}_S|\boldsymbol{x}\mathrm{d}\mu_S(\boldsymbol{x})}{\int_S |\boldsymbol{u}(t,\boldsymbol{x})\cdot\boldsymbol{n}_S|\mathrm{d}\mu_S(\boldsymbol{x})},$$

we define the NFD as the distance of the normal flow moment from the centroid $\boldsymbol{x}_S$, normalized by the hydraulic radius $r_H(S) = \frac{|S|}{|\partial S|}$:

$$\mathrm{NFD}_S(t) := \frac{|\boldsymbol{x}_{\mathrm{n}}\big(\boldsymbol{u}(t,\cdot),S\big) - \boldsymbol{x}_S|}{r_H(S)}.$$

The NFD is a dimensionless number ranging from $0$ (perfectly centered flow) to $\frac{R(S)}{r_H(S)}$, where $R(S) = \max_{\boldsymbol{x}\in S} = |\boldsymbol{x} - \boldsymbol{x}_S|$ is the geometric radius. This upper limit is not approached very closely in physiological flows, however.

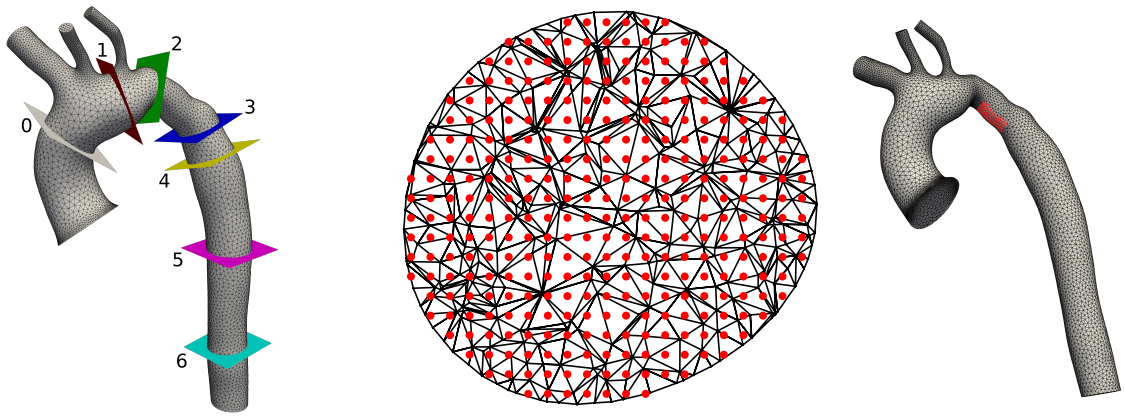


Figure 4: Left: positions of the planar cross-sections $S_0$ through $S_6$ of the aorta segment under consideration. Center: quadrature points on a coarse $1\,\mathrm{mm}$-resolution grid on cross-section 4. Right: reference patch for wall shear stress computation.

### 3.5 Wall Shear Stress (WSS) and Oscillatory Shear Index (OSI)

The wall shear stress (WSS) quantifies the density of tangential force exerted by the passing flow on the walls of the blood vessel. At a given point $\boldsymbol{x} \in \partial\Omega$ on the boundary, with unit outer normal $\boldsymbol{n}$, the WSS at $\boldsymbol{x}$ is given by the normal derivative of the tangential component of the velocity at $\boldsymbol{x}$ multiplied by the dynamic viscosity:

$$\tau_{\mathrm{w}}(t,\boldsymbol{x}) = \mu \frac{\partial}{\partial \boldsymbol{n}} \Big( \boldsymbol{u}(t,\boldsymbol{x}) - \big(\boldsymbol{u}(t,\boldsymbol{x}) \cdot \boldsymbol{n}\big)\boldsymbol{n} \Big).$$

As the WSS is a tangential pressure, it is essentially a two-dimensional quantity. Given a constant unit vector $\boldsymbol{v}$ representing a generally forward direction near a region of interest, the WSS decomposes into a forward (or backward) component $\tau_{\mathrm{w,f}} = \tau_{\mathrm{w}} \cdot \boldsymbol{v}$ and a lateral component $\tau_{\mathrm{w,l}} = \tau_{\mathrm{w}} \cdot \boldsymbol{w}$, where $\boldsymbol{w} = \boldsymbol{w}(\boldsymbol{x})$ is a unit vector orthogonal to both $\boldsymbol{v}$ and the outer unit normal $\boldsymbol{n}(\boldsymbol{x})$. As the sign of $\tau_{\mathrm{w,l}}$ depends on the orientation of $\boldsymbol{w}$, when comparing spatially averaged quantities we will instead consider its magnitude $|\tau_{\mathrm{w,l}}| = |\tau_{\mathrm{w}} - (\tau_{\mathrm{w}} \cdot \boldsymbol{v})\boldsymbol{v}|$.

The oscillatory shear index (OSI) measures the extent to which the WSS oscillates, as quantified by the relative difference between the magnitude of the temporal mean of the WSS vector and the temporal mean of its magnitude:

$$\mathrm{OSI}_I(\boldsymbol{x}) = \frac{1}{2}\left(1 - \frac{\left|\int_I \tau_{\mathrm{w}}(t,\boldsymbol{x})\mathrm{d}t\right|}{\int_I |\tau_{\mathrm{w}}(t,\boldsymbol{x})|\mathrm{d}t}\right),$$

where $\boldsymbol{x} \in \partial\Omega$ is a point on the boundary and $I$ is a time interval of interest, e.g., a single heartbeat or a longer simulation period spanning multiple heartbeats.

### 3.6 Regions of Interest

We evaluate average pressure, SFD, and NFD on seven cross-sections $S_i$ of the domain, as shown in Figure 4 (left), for $i = 0, \ldots, 6$. Notice that $S_i$ includes only the connected component of the intersection of $\Omega$ with the defining plane closest to the depicted portions of the planes. They are placed in key positions along the aorta segment, namely:

$S_0$: just past the inlet boundary, as the ascending aorta curves into the aortic arch,

$S_1$: at the center of the aortic arch, before the left common subclavian artery,

$S_2$: between the left common subclavian artery and the coarctation,

$S_3$: past the coarctation where the aortic arch straightens into the descending aorta,

$S_4$: close to the upper end of the descending aorta,

$S_5$: half-way between the coarctation and the outlet boundary, and

$S_6$: close to the outlet boundary,

Each of these quantities involves the evaluation of integrals over the cross-section. We chose to approximate these integrals using a regular Cartesian grid of quadrature point on each cross-section $S_i$. Choosing two orthogonal unit vectors $\boldsymbol{t}_i$ and $\boldsymbol{t}_i'$ tangential to $S_i$, a central point $\boldsymbol{x}_i \in S_i$ and the resolution $h^{(q)} = 0.1\,\mathrm{mm}$, we associate each point

$$\boldsymbol{x}_{i,km}^{(q)} = \boldsymbol{x}_i + kh^{(q)}\boldsymbol{t}_i + mh^{(q)}\boldsymbol{t}_i' \in S_i,\ k, m \in \mathbb{Z},$$

with the constant weight $(h^{(q)})^2 = 100\,\mu\mathrm{m}^2$. Figure 4 (center) shows a coarser $1\,\mathrm{mm}$ grid on cross-section 4, by way of example. The velocity extremes on a cross-section $S_i$ are estimated using the same points. To estimate the maximum velocity in the wedge $W_i$ between cross-sections $S_i$ and $S_{i+1}$, $i = 0, \ldots, 5$, the velocity is estimated on the bounding cross-sections and on all vertices and edge, face, and cell midpoints within $W_i$.

In Figure 4 (right), a patch on the underside of the aorta is highlighted, which is the region of interest for studying the wall shear stress because it is just past the exit of the coarctation, where a jet is expected to form. In the space between the jet and the underside of the aorta, there should be noticeable vortex formation, causing backward or oscillating shear stress on the reference patch.

# 4 Numerical Studies

## 4.1 Setup of the Simulations

We performed simulations with each of the viscosity models listed in Section 2.4 paired with both the $\boldsymbol{\sigma}$-model (Section 2.5.1) and the RB-VMS model (Section 2.5.2). Since the $\boldsymbol{\sigma}$-model does not contain a pressure stabilization, and we did not add such a term, the finite element velocity and pressure space have to satisfy a discrete inf-sup condition. We used Taylor–Hood finite elements on the base mesh $\mathcal{T}$, i.e., $\boldsymbol{V}_h = \mathrm{P}_2(\mathcal{T})^3$, $Q_h = \mathrm{P}_1(\mathcal{T})$, which is the most widely used inf-sup stable pair of spaces. As the RB-VMS model naturally includes a pressure-pressure term, it does not require an inf-sup stable pair of finite element spaces. We used piecewise linear velocities and pressures on the uniformly refined mesh $\mathcal{T}'$, i.e., $\boldsymbol{V}_h = \mathrm{P}_1(\mathcal{T}')^3$, $Q_h = \mathrm{P}_1(\mathcal{T}')$. Table 3 lists the sizes of these spaces. Note that $\dim \mathrm{P}_1(\mathcal{T}') = \dim \mathrm{P}_2(\mathcal{T})$, so that the velocity spaces have the same dimension in both cases.

We discretized in time using a BDF-2 scheme with a fixed time step length of $\Delta t = 125\,\mu\mathrm{s}$. The resulting nonlinear systems were solved using a Picard iteration (see (6), (8), (15) for an overview of the linearization), terminating the iteration when the Euclidean norm of the residual vector no longer

Table 3: Information on the mesh and the velocity/pressure space dimensions.

| Mesh | Tetrahedra | $\dim(\mathrm{P}_1)$ | $\dim(\mathrm{P}_2)$ | $\dim(\mathrm{P}_1^3 \times \mathrm{P}_1)$ | $\dim(\mathrm{P}_2^3 \times \mathrm{P}_1)$ |
|---|---|---|---|---|---|
| $\mathcal{T}$ | $106,983$ | $21,495$ | $158,335$ | – | $496,500$ |
| $\mathcal{T}'$ | $855,864$ | $158,335$ | – | $633,340$ | – |

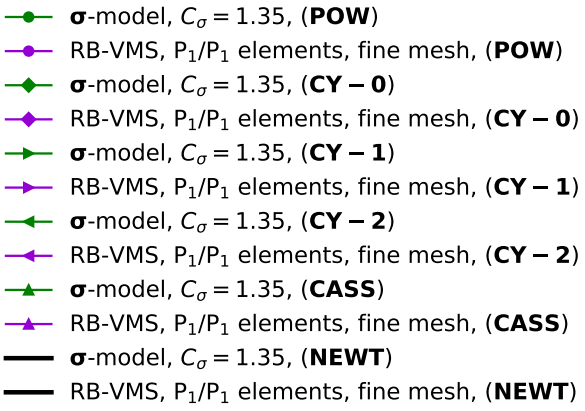


Figure 5: Common legend for plots showing the impact of the variation of viscosity and turbulence models.

exceeded $10^{-10}$. All simulations were run on the time interval $[0, T]$ with $T = 11\,\mathrm{s}$, covering 11 heartbeats. We will compare ranges and averages over the latter 10 heartbeats, discarding the first period to avoid artifacts due to the homogeneous initial conditions.

The linear systems corresponding to each step of the Picard iteration were solved by FGMRES iteration, using a least-squares commutator preconditioner[2] (as proposed in [25]) for the simulations using the $\boldsymbol{\sigma}$-model and a hybrid FGMRES/BiCGSTAB approach for the RB-VMS computations[3].

The simulations were run using the finite element library ParMooN [27] developed at WIAS Berlin, using 32 parallel processes per simulation on several HPE Synergy 660 Gen10 compute servers with four Intel Xeon Gold 6254 CPUs, each with 18 cores clocked at 3.1 GHz.

Figure 5 shows the common legend for each of the figures below. In each time-averaged plot (e.g., Figure 7, left) the line corresponding to the legend shows the average over the whole time interval $[1, 11]\,\mathrm{s}$. Each time-dependent plot (e.g., Figure 7, right) presents the period-average of the given quantity at the instant $t$ in the sense of averaging over $t + i$, $i = 1, \ldots, 10$. Period-by-period variation is omitted, as it would make the graphs difficult to interpret; however, in the case of the RB-VMS model's computations, it is in any case not significant. The $\boldsymbol{\sigma}$-model does show substantial variation from period to period e.g. for the NFD at very low flow rates (e.g. Figure 10, upper right, $t$ between $0.25$ and $0.5\,\mathrm{s}$), but this has little impact on the averaged results; see [4] for more information in the

[2] This involves solving two relatively low-dimensional pressure-block systems for the approximate Schur complement inversion; we used the parallel sparse direct solver MUMPS for this purpose. The larger velocity-block problems were solved using the same FGMRES/BiCGSTAB approach used for the RB-VMS systems, except in the cases of (**CASS**) and (**POW**), where BiCGSTAB was poorly behaved and a simple Jacobi preconditioner was used instead.

[3] The least-squares commutator approach is specific to saddle point problems as encountered in non-stabilized discretizations. Although extensions to stabilized problems have been proposed, e.g., in [26], these performed poorly when applied to the systems resulting from our RB-VMS discretization.

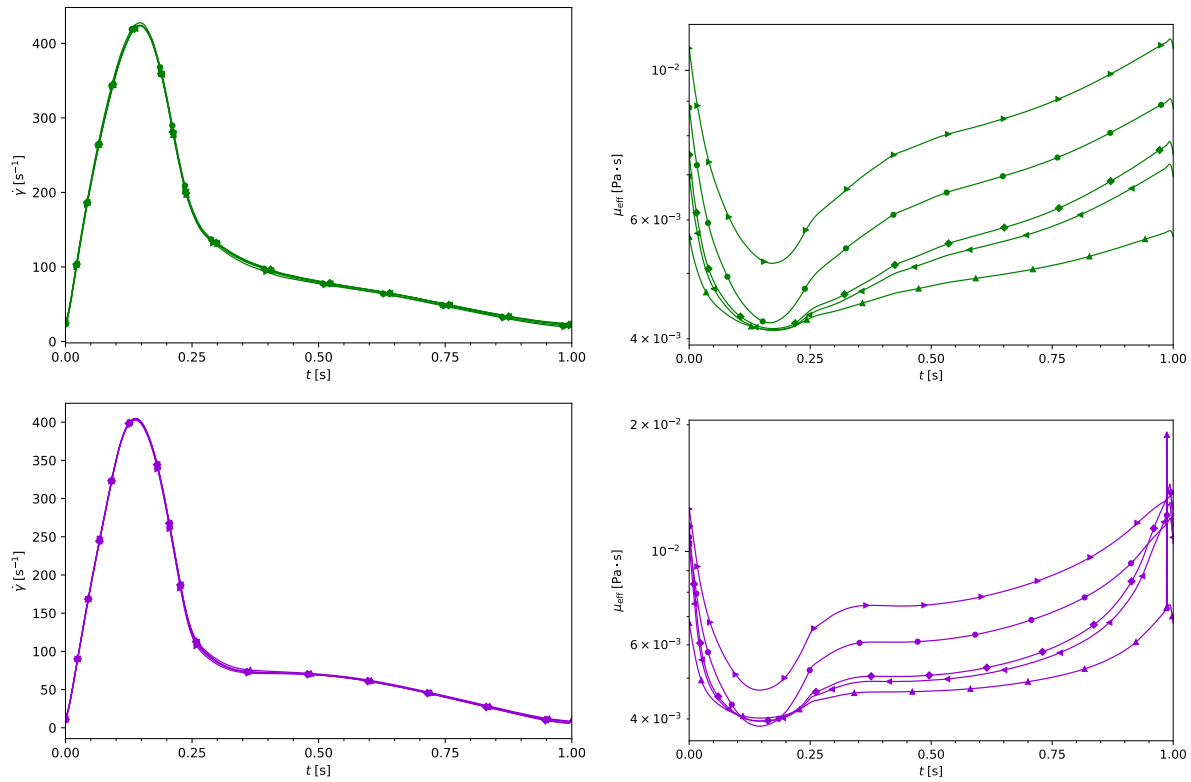


Figure 6: Impact of the variation of viscosity and turbulence models on shear rates and viscosities. Top: $\boldsymbol{\sigma}$-model. Bottom: RB-VMS model. Left: Shear rate averaged over the whole domain. Right: Effective viscosity averaged over the whole domain. Legend in Figure 5.

Newtonian case.

## 4.2 Viscosity

Figure 6 presents the volume-averaged shear rates and effective viscosities for each model. Notice that the viscosities vary by less than an order of magnitude, and the difference in shear rates is barely detectable, even though the more rapid decay of high-frequency modes under the RB-VMS model causes the viscosity in some regions to spike near the end of diastole when combined with (**CASS**), as seen in the lower right-hand figure.

## 4.3 Pressure Difference

Results for the pressure difference are depicted in Figure 7. On the left-hand side, the time-averaged pressure difference over each cross-section relative to cross-section 0 is presented and on the right-hand side the period-averaged pressure difference between cross-sections 6 and 2, with the clinical threshold of $20\,\mathrm{mmHg}$ for the trans-stenotic pressure difference highlighted. The choice of the viscosity model possesses a negligible impact on the time-averaged pressure differences, though (**POW**)is a slight outlier within the $\boldsymbol{\sigma}$-model computations. Noting the different scales of the ordinate for the pressure differences between the cross-sections, one can see that the choice of the turbulence model has a tremendous impact instead.

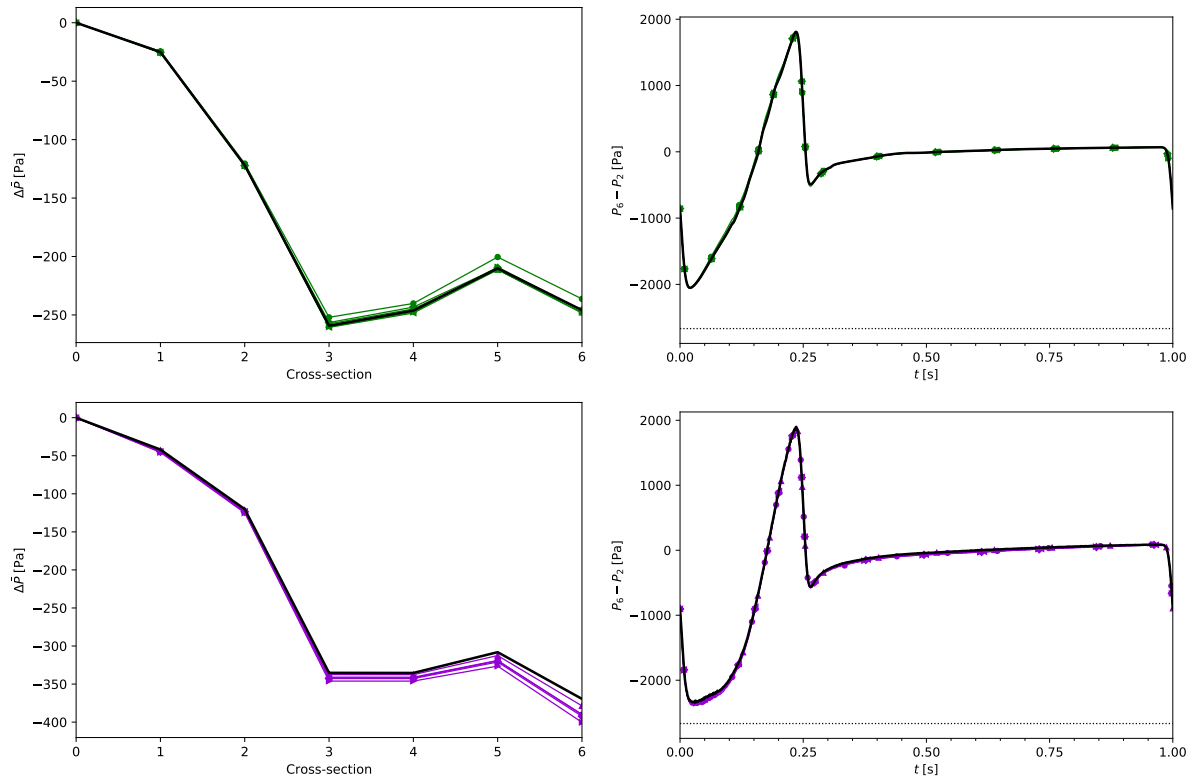


Figure 7: Impact of the variation of viscosity and turbulence models on the pressure difference. Top: $\boldsymbol{\sigma}$-model. Bottom: RB-VMS model. Left: time-averaged pressure difference on each cross-section. Right: pressure difference between cross-sections 6 and 2 over time. The $20\,\mathrm{mmHg}$ threshold marked by a dotted line. Note the different scalings of the ordinate in the left pictures. Legend in Figure 5.

## 4.4 Maximum Velocity

Comparisons of the maximum velocity in the wedge $W_2$ between cross-sections 2 and 3 and through cross-section 6 are shown in Figure 8. Again, the choice of the turbulence model is of much more importance than the choice of the viscosity model. Whereas all curves are more or less on top of each other for the RB-VMS model, slight variations can be observed for the $\boldsymbol{\sigma}$-model on cross-section 6.

## 4.5 Secondary Flow Degree

Figure 9 depicts the time-averaged SFD across each cross-section (left) and the period-averaged SFD across cross-section 4 (right). Although the choice of turbulence model is also for this biomarker of greater impact than the choice of the viscosity model, one can observe also a notable impact of the latter for each turbulence model. A broad tendency toward smaller SFD with the various non-Newtonian models may be observed, as each is somewhat more viscous in the relevant range of shear rates than the Newtonian model. The model (**CY-1**), which has the highest viscosity over most of this range, exhibits often the smallest SFD.

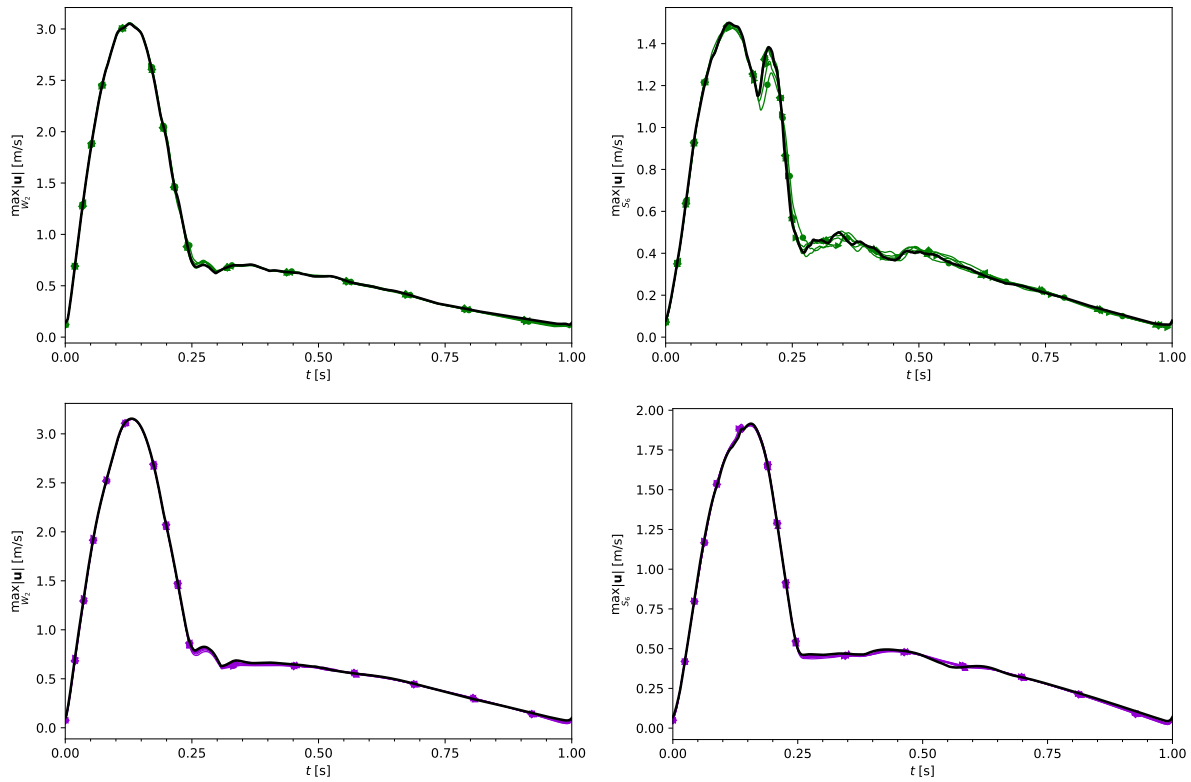


Figure 8: Impact of the variation of viscosity and turbulence models on the maximum velocity. Top: $\boldsymbol{\sigma}$-model. Bottom: RB-VMS model. Left: Maximum velocity in the wedge $W_2$ between cross-sections 2 and 3 over time. Right: Maximum velocity through cross-section 6 over time. Legend in Figure 5.

## 4.6 Normalized Flow Displacement

The time-averaged NFD across each cross-section and the period-averaged NFD across cross-section 4 are displayed in Figure 10. Again, the impact of modelling the turbulence dominates the influence of the viscosity model. Slight variations depending on the viscosity model can be observed for the NFD behavior during a period.

## 4.7 Wall Shear Stress

Results obtained for the wall shear stress's magnitude and the forward component, averaged over the reference patch highlighted in Figure 4, are given in Figure 11. Because of the substantial difference in behavior at walls of the two turbulence models, this choice proved to be much more influential once again. But within each turbulence model, also the impact of viscosity modeling is visible, e.g., the averaged WSS magnitude over the reference patch is usually somewhat larger for the non-Newtonian models than for the Newtonian one, in particular for (**CY-1**). The notable exception to this is (**POW**) during systole, which can be seen in Figure 3 to have particularly small viscosities at high shear rates.

Table 4 lists the time-averaged wall shear stress magnitude and oscillatory shear index averaged over the reference patch for each model. As expected, the influence of the choice of turbulence model again greatly exceeds the viscosity model's.

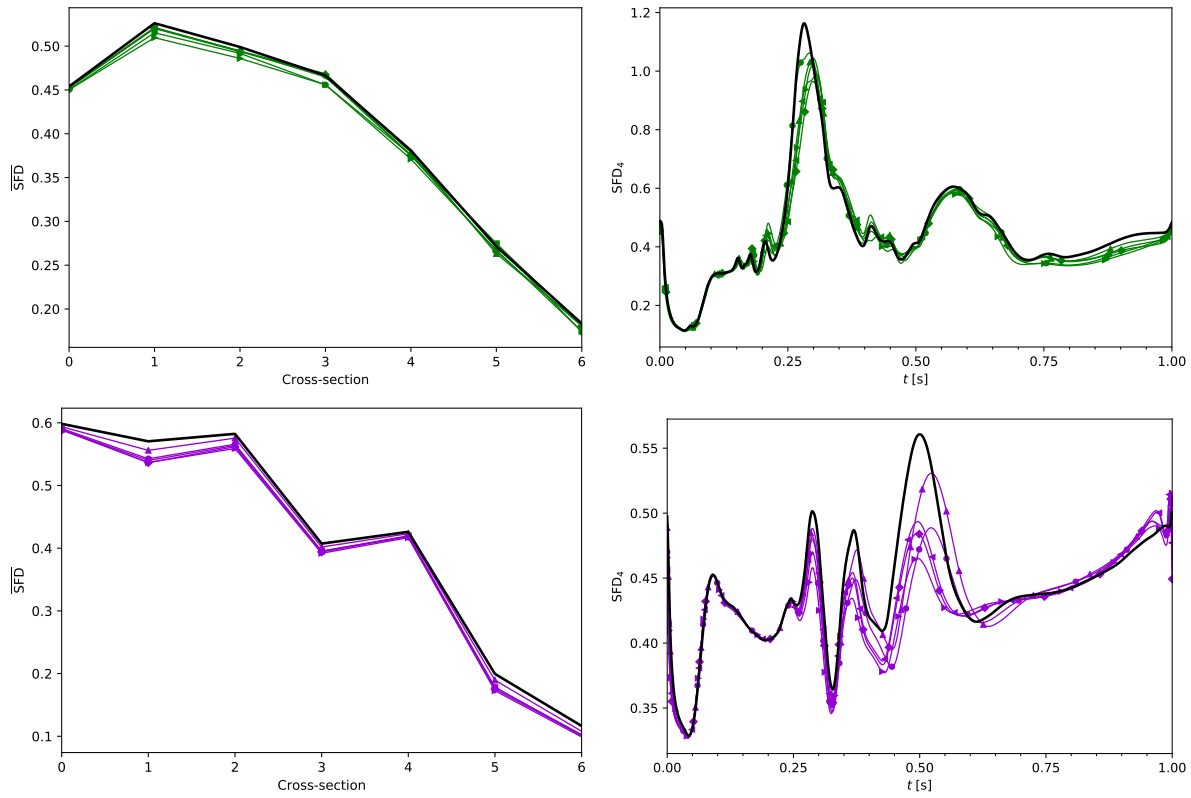


Figure 9: Impact of the variation of viscosity and turbulence models on the SFD. Top: $\boldsymbol{\sigma}$-model. Bottom: RB-VMS model. Left: Time-averaged secondary flow degree. Right: Secondary flow degree across cross-section 4 over time. Note the different scalings of the ordinate in the right pictures. Legend in Figure 5.

Table 4: Information on the time-averaged wall shear stress magnitude and OSI.

| Model | $\mu(\lvert\tau_{\mathrm{w}}\rvert)$ [Pa] | OSI |
|---|---|---|
| $\boldsymbol{\sigma}$-model, (**NEWT**) | 1.185 | 0.309 |
| $\boldsymbol{\sigma}$-model, (**POW**) | 1.061 | 0.327 |
| $\boldsymbol{\sigma}$-model, (**CY-0**) | 1.290 | 0.313 |
| $\boldsymbol{\sigma}$-model, (**CY-1**) | 1.264 | 0.322 |
| $\boldsymbol{\sigma}$-model, (**CY-2**) | 1.256 | 0.313 |
| $\boldsymbol{\sigma}$-model, (**CASS**) | 1.186 | 0.320 |
| RB-VMS, (**NEWT**) | 0.534 | 0.246 |
| RB-VMS, (**POW**) | 0.584 | 0.226 |
| RB-VMS, (**CY-0**) | 0.589 | 0.237 |
| RB-VMS, (**CY-1**) | 0.686 | 0.228 |
| RB-VMS, (**CY-2**) | 0.588 | 0.238 |
| RB-VMS, (**CASS**) | 0.616 | 0.236 |

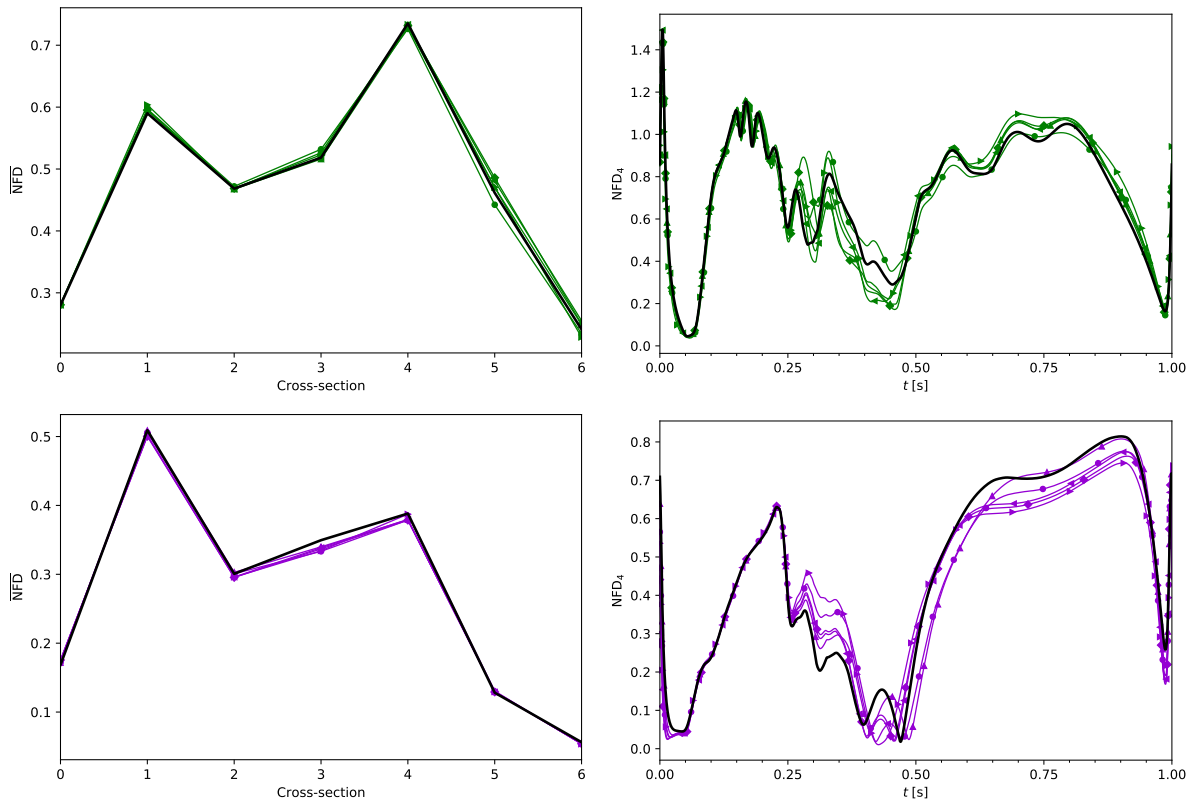


Figure 10: Impact of the variation of viscosity and turbulence models on the NFD. Top: $\boldsymbol{\sigma}$-model. Bottom: RB-VMS model. Left: Time-averaged normalized flow displacement. Right: Normalized flow displacement across cross-section 4 over time. Note the different scalings of the ordinates for both turbulence models. Legend in Figure 5.

## 4.8 Computational Costs

Figure 12 compares the number of iterations taken by each model to achieve the stopping criteria stated in Section 4.1. Each plot shows (for legibility) a running average over 10 output steps (i.e. 80 computed time steps) of the number of Picard iterations[4] (left) and the total number of FGMRES iterations[5] (right), further averaged over the latter ten periods.

It is clear that by these metrics, the $\boldsymbol{\sigma}$-model's iteration counts differ very little, whereas in the RB-VMS case, additional Picard iterations (and consequently linear solver iterations) were often required specifically in the (**CASS**) and (**POW**) settings, particularly during systole, with clearly visible peaks during acceleration and deceleration and a smaller peak at peak flow. This was not the case for the $\boldsymbol{\sigma}$-model and is perhaps due to the smoother velocity fields computed by the RB-VMS model, giving larger areas with slow shear rates below $10\,\mathrm{s}^{-1}$, where the effective viscosity according to (**CASS**) and (**POW**) is large and changes rapidly with respect to the shear rate.

Actual computation times of the different models are difficult to compare, as varying load due to other tasks on the same servers caused additional variation in runtime. Nevertheless, average CPU times

[4] Note that as the final Picard iteration always consists solely of assembly of the linear system and computation of the residual at the previous iteration's result, a single iteration can be achieved only in the unusual case when the initial guess's residual is already small enough. This did not occur in our simulations.

[5] That is, the number of the (outer) linear solver's iterations summed up over all Picard iterations for a given time step.

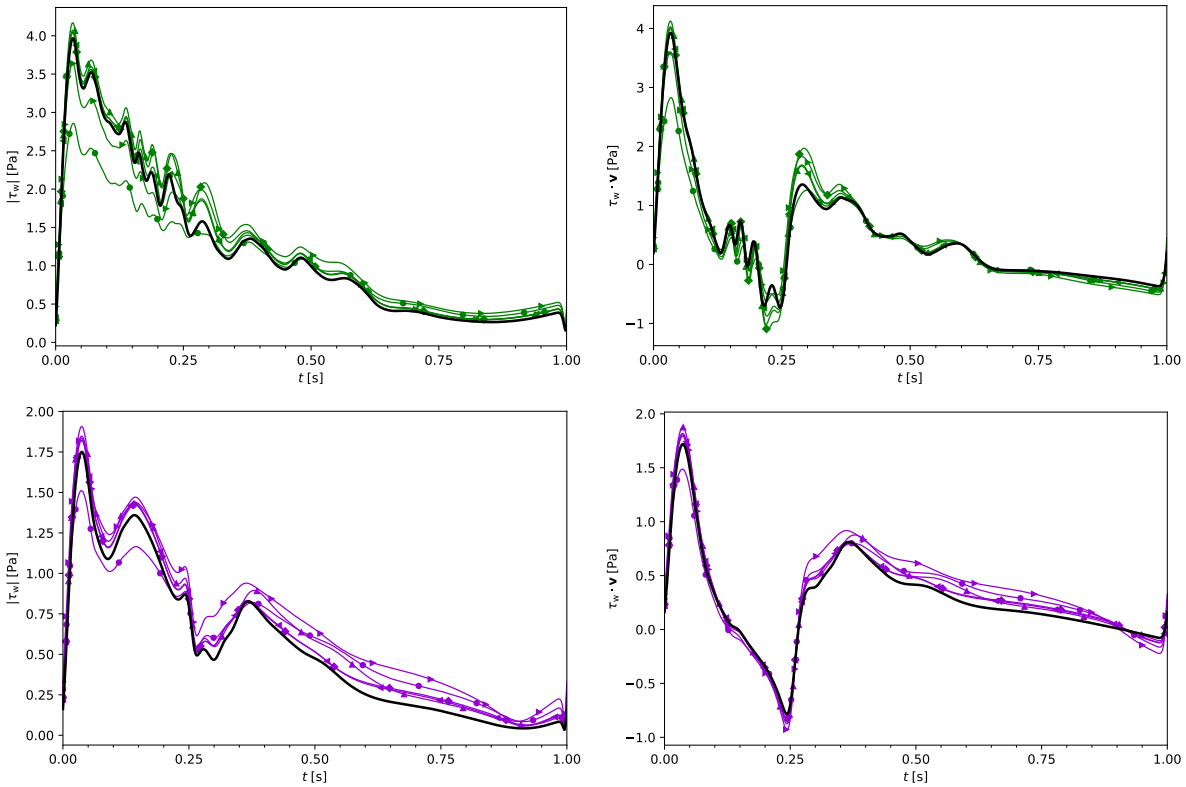


Figure 11: Impact of the variation of viscosity and turbulence models on the WSS. Top: $\boldsymbol{\sigma}$-model. Bottom: RB-VMS model. Left: Wall shear stress magnitude averaged over reference patch. Right: Forward wall shear stress averaged over reference patch. Note the different scalings of the ordinates for both turbulence models. Legend in Figure 5.

per millisecond simulated (that is, per 8 simulated time steps) were on the order of $26.5 - 43.0\,\mathrm{s}$ for the $\boldsymbol{\sigma}$-model and $60.2 - 73.1\,\mathrm{s}$ for the RB-VMS model.

# 5 Conclusions

This paper studied the impact of viscosity modeling and of choosing the turbulence model in generalized Newtonian blood flow simulations in an aortic coarctation. For all clinically relevant biomarkers that were monitored, the impact of the numerical modeling with the turbulence model dominated the impact of the physical viscosity modeling. For time-averaged quantities defined on cross-sections of the aorta, the differences of the results between different viscosity models within the simulations with the same turbulence model were negligible. The instantaneous behavior, averaged over the periods, showed, in some cases, minor quantitative differences among the viscosity models, e.g., for the secondary flow degree, the normalized flow displacement, and the wall shear stress. However, the order of magnitude of these differences is not expected to affect diagnostic decisions.

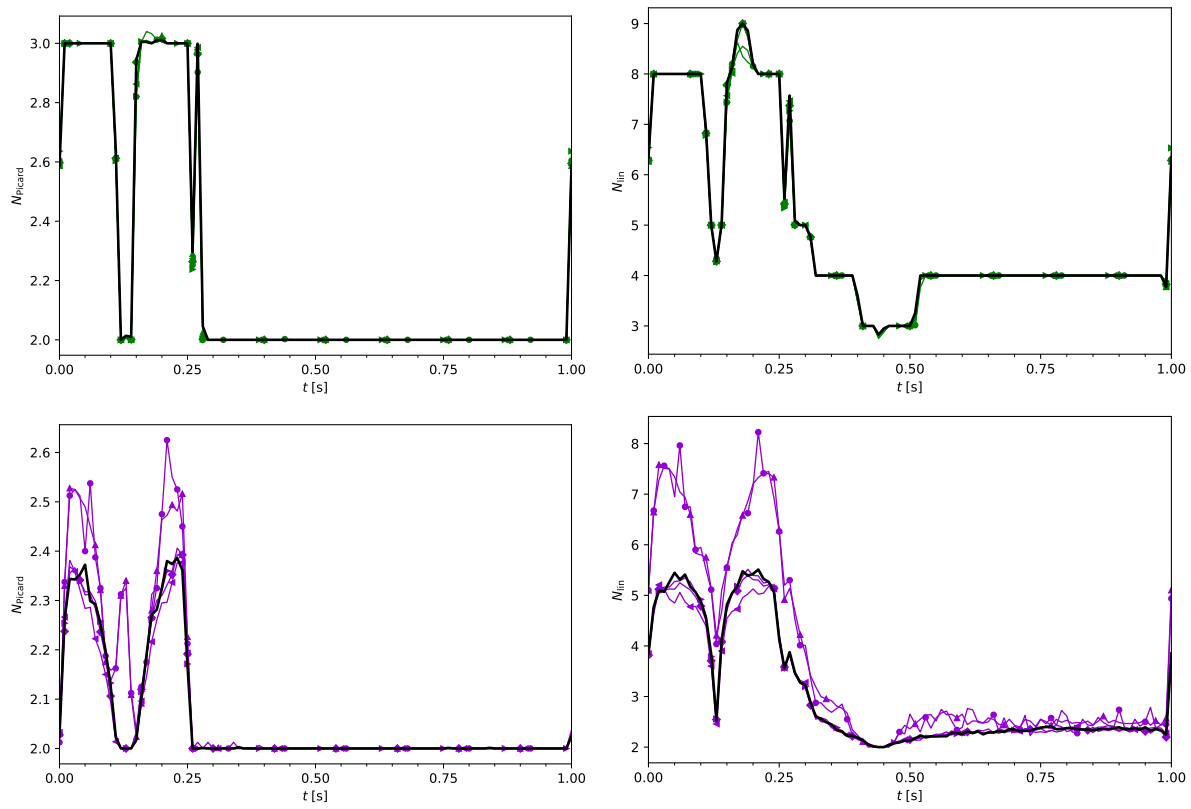


Figure 12: Impact of the variation of viscosity and turbulence models on computation efficiency. Top: $\sigma$-model. Bottom: RB-VMS model. Left: Average number of Picard iterations per time step. Right: Average number of (outer) linear solver iterations per time step. Legend in Figure 5.

## References

[1] J. C. Nielsen, A. J. Powell, K. Gauvreau, E. N. Marcus, A. Prakash, T. Geva, Magnetic Resonance Imaging Predictors of Coarctation Severity, Circulation 111 (2005) 622–628.

[2] L. Goubergrits, E. Riesenkampff, P. Yevtushenko, J. Schaller, U. Kertzscher, A. Hennemuth, F. Berger, S. Schubert, T. Kuehne, Mri-based computational fluid dynamics for diagnosis and treatment prediction: Clinical validation study in patients with coarctation of aorta, Journal of Magnetic Resonance Imaging 41 (4) (2015) 909–916.

[3] C. Schubert, J. Brüning, L. Goubergits, A. Hennemuth, F. Berger, T. Kühne, M. Kelm, Assessment of hemodynamic responses to exercise in aortic coarctation using mri-ergometry in combination with computational fluid dynamics, Scientific reports 10 (2020) 18894.

[4] S. Katz, A. Caiazzo, B. Moreau, U. Wilbrandt, J. Brüning, L. Goubergrits, V. John, Impact of turbulence modeling on the simulation of blood flow in aortic coarctation, Tech. Rep. arXiv:2208.14217, arXiv, submitted (2022). arXiv:2208.14217[physics], doi:10.48550/arXiv.2208.14217.

[5] M. A. Elblbesy, A. T. Hereba, Computation of the coefficients of the power law model for whole blood and their correlation with blood parameters, Applied Physics Research 8 (2) (2016) 1. doi:10.5539/apr.v8n2p1.

[6] A. Sequeira, J. Janela, An overview of some mathematical models of blood rheology, in: M. S. Pereira (Ed.), A Portrait of State-of-the-Art Research at the Technical University of Lisbon, Springer Netherlands, 2007, pp. 65–87. doi:10.1007/978-1-4020-5690-1_4.

[7] J. Bernsdorf, D. Wang, Non-Newtonian blood flow simulation in cerebral aneurysms, Computers & Mathematics with Applications 58 (5) (2009) 1024–1029. doi:10.1016/j.camwa.2009.02.019.

[8] F. Abraham, M. Behr, M. Heinkenschloss, Shape optimization in steady blood flow: a numerical study of non-Newtonian effects, Computer Methods in Biomechanics and Biomedical Engineering 8 (2) (2005) 127–137. doi:10.1080/10255840500180799.

[9] H. G. Morales, I. Larrabide, A. J. Geers, M. L. Aguilar, A. F. Frangi, Newtonian and non-Newtonian blood flow in coiled cerebral aneurysms, Journal of Biomechanics 46 (13) (2013) 2158–2164. doi:10.1016/j.jbiomech.2013.06.034.

[10] C.-H. Bruneau, P. Fabrie, New efficient boundary conditions for incompressible navier-stokes equations: a well-posedness result, ESAIM: Mathematical Modelling and Numerical Analysis 30 (7) (1996) 815–840. doi:10.1051/m2an/1996300708151.

[11] M. Braack, P. B. Mucha, Directional do-nothing condition for the navier-stokes equations, Journal of Computational Mathematics 32 (5) (2014) 507–521. doi:10.4208/jcm.1405-m4347.

[12] M. E. Klingensmith, L. E. Chen, S. C. Glasgow, T. A. Goers, S. J. Melby, The Washington Manual of Surgery, 5th Edition, Wolters Kluwer Health / Lippincott Williams & Wilkins, 2008.

[13] H. Liu, L. Lan, J. Abrigo, H. L. Ip, Y. Soo, D. Zheng, K. S. Wong, D. Wang, L. Shi, T. W. Leung, X. Leng, Comparison of newtonian and non-newtonian fluid models in blood flow simulation in patients with intracranial arterial stenosis, Frontiers in Physiology 12 (2021) 718540. doi:10.3389/fphys.2021.718540.

[14] R. Perinajová, J. F. Juffermans, J. L. Mercado, J.-P. Aben, L. Ledoux, J. J. M. Westenberg, H. J. Lamb, S. Kenjereš, Assessment of turbulent blood flow and wall shear stress in aortic coarctation using image-based simulations, BioMedical Engineering OnLine 20 (1) (2021) 84. doi:10.1186/s12938-021-00921-4.

[15] A. Zingaro, I. Fumagalli, L. Dede, M. Fedele, P. C. Africa, A. F. Corno, A. Quarteroni, A geometric multiscale model for the numerical simulation of blood flow in the human left heart, Discrete and Continuous Dynamical Systems - S 15 (8) (2022) 2391. doi:10.3934/dcdss.2022052.

[16] W. Ostwald, Über die rechnerische Darstellung des Strukturgebietes der Viskosität, Kolloid-Zeitschrift 47 (2) (1929) 176–187. doi:10.1007/BF01496959.

[17] K. Yasuda, Investigation of the analogies between viscometric and linear viscoelastic properties of polystyrene fluids, Thesis (Ph.D.), Massachusetts Institute of Technology (1979).

[18] P. J. Carreau, Rheological equations from molecular network theories, Transactions of the Society of Rheology 16 (1) (1972) 99–127, publisher: The Society of Rheology. doi:10.1122/1.549276.

[19] N. Casson, Rheology and the letterpress printing process, Journal of the Society of Dyers and Colourists 69 (13) (1953) 576–582. doi:10.1111/j.1478-4408.1953.tb02800.x.

[20] G. W. S. Blair, An equation for the flow of blood, plasma and serum through glass capillaries, Nature 183 (4661) (1959) 613–614, number: 4661 Publisher: Nature Publishing Group. doi:10.1038/183613a0.

[21] F. Nicoud, H. B. Toda, O. Cabrit, S. Bose, J. Lee, Using singular values to build a subgrid-scale model for large eddy simulations, Physics of Fluids 23 (8) (2011) 085106. doi:10.1063/1.3623274.

[22] Y. Bazilevs, V. Calo, J. Cottrell, T. Hughes, A. Reali, G. Scovazzi, Variational multiscale residual-based turbulence modeling for large eddy simulation of incompressible flows, Computer Methods in Applied Mechanics and Engineering 197 (1) (2007) 173–201. doi:10.1016/j.cma.2007.07.016.

[23] N. Ahmed, T. Chacón Rebollo, V. John, S. Rubino, A review of variational multiscale methods for the simulation of turbulent incompressible flows, Arch. Comput. Methods Eng. 24 (1) (2017) 115–164. doi:10.1007/s11831-015-9161-0.
URL http://dx.doi.org/10.1007/s11831-015-9161-0

[24] V. John, Finite element methods for incompressible flow problems, Vol. 51 of Springer Series in Computational Mathematics, Springer, Cham, 2016. doi:10.1007/978-3-319-45750-5.

[25] H. Elman, V. E. Howle, J. Shadid, R. Shuttleworth, R. Tuminaro, Block preconditioners based on approximate commutators, SIAM Journal on Scientific Computing 27 (5) (2006) 1651–1668. doi:10.1137/040608817.

[26] H. Elman, V. E. Howle, J. Shadid, D. Silvester, R. Tuminaro, Least squares preconditioners for stabilized discretizations of the navier–stokes equations, SIAM Journal on Scientific Computing 30 (1) (2008) 290–311. doi:10.1137/060655742.

[27] U. Wilbrandt, C. Bartsch, N. Ahmed, N. Alia, F. Anker, L. Blank, A. Caiazzo, S. Ganesan, S. Giere, G. Matthies, R. Meesala, A. Shamim, J. Venkatesan, V. John, ParMooN—A modernized program package based on mapped finite elements, Comput. Math. Appl. 74 (1) (2017) 74–88. doi:10.1016/j.camwa.2016.12.020.